Tectonophysics 834 (2022) 229355

Contents lists available at ScienceDirect

Tectonophysics

journal homepage: www.elsevier.com/locate/tecto

Paleoseismic evidence of the 1715 C.E earthquake on the Purgatorio Fault in Southern Peru: Implications for seismic hazard in subduction zones

Carlos Benavente [a,b,*], Anderson Palomino [a], Sam Wimpenny [c], Briant García [a], Lorena Rosell [a], Enoch Aguirre [a], José Macharé [d], Alba M. Rodriguez Padilla [e], Sarah R. Hall [f]

[a] Instituto Geológico, Minero y Metalúrgico INGEMMET, San Borja, Peru
[b] Especialidad Ingeniería Geológica, Facultad de Ciencias e Ingeniería, Pontificia Universidad Católica del Perú, Av. Universitaria 1801, San Miguel, Lima 15088, Peru
[c] COMET, Bullard Laboratories, Department of Earth Sciences, University of Cambridge, UK
[d] National University of Engineering, Peru
[e] Department of Earth and Planetary Science, University of California, Davis, USA
[f] Environmental Science, College of the Atlantic, Bar Harbor, Maine, USA

ARTICLE INFO

Keywords:
Forearc crustal earthquakes
Subduction zones
Geomorphology
Palaeoseismology
Historical earthquake

ABSTRACT

Active faults in the forearc of southern Peru pose a poorly understood hazard to the region. The Purgatorio Fault is a 60 km-long fault that extends between Moquegua and Tacna that has hosted several scarp-forming earthquakes over the last 6 ka. We present new measurements of the fault scarp geomorphology along the Purgatorio Fault, and use dating of the stratigraphy within a new paleoseismic trench excavated across the fault to establish the chronology of scarp formation. We find that the most recent surface-rupturing earthquake on the Purgatorio Fault occurred sometime between 1630C.E and 1790C.E and had a moment magnitude (M_w) of ~7. We propose that this most recent surface-rupturing earthquake on the Purgatorio Fault was the 1715C.E earthquake recorded in the historical catalogue of the region, which was previously attributed to the megathrust offshore. Our results highlight the importance of establishing a paleoseismic record of onshore faults to differentiate between major megathrust and forearc earthquakes. Given the proximity of these shallow, onshore faults to coastal communities in Peru, the shallow earthquakes they generate may pose a severe, yet often overlooked, seismic hazard.

1. Introduction

The historical record of earthquake shaking in coastal regions adjacent to subduction zones provides important information for estimating the timing, extent and magnitude of past megathrust earthquakes (Dorbath et al., 1990). One approach to quantifying the hazard associated with future megathrust earthquakes is to combine the historical record of large earthquake ruptures with modern geodetic measurements of the slip-rate deficit to estimate the total slip deficit at different points along the subduction interface (e.g. Villegas-Lanza et al., 2016). Where the slip deficit is largest, the possibility of a future megathrust earthquake is generally inferred to be high. Another approach is to compile the along-strike extent of historical megathrust ruptures to infer the presence of persistent 'barriers' on the megathrust that may limit the rupture area of future earthquakes (Dorbath et al., 1990). Ultimately, both methods rely on the accuracy of the historical record of earthquake shaking, and its interpretation, for identifying the along-strike extent and magnitude of past megathrust earthquakes. However, identifying megathrust earthquakes from the historical shaking record is complicated by the fact that shallow faults in the forearc can also host large earthquakes of $M_w > 7$ (Hall et al., 2008; Audin et al., 2006; Benavente and Audin, 2009; Benavente et al., 2021). Forearc earthquakes will rupture faults that dip steeply through the wedge of rock overlying the megathrust, and may reach the surface either on land or offshore. Misidentification of large forearc earthquakes as megathrust events can, therefore, lead to inaccurate hazard estimates for both megathrust and forearc faults. For example, while a megathrust earthquake may pose a larger coastal tsunami hazard, a shallow earthquake on an onshore forearc fault may pose a larger shaking hazard to communities living further inland from the coast.

Subduction of the Nazca Plate beneath the western margin of South America has generated a series of large megathrust earthquakes within southern Peru, most recently in the Mw 8.42001 Arequipa earthquake (Pritchard et al., 2007). The rupture areas and magnitudes of these past

* Corresponding author at: Instituto Geológico, Minero y Metalúrgico INGEMMET, Av. Canadá, 1470 San Borja Lima, Peru.
E-mail address: cbenavente@ingemmet.gob.pe (C. Benavente).

https://doi.org/10.1016/j.tecto.2022.229355
Received 10 November 2021; Received in revised form 5 April 2022; Accepted 11 April 2022
Available online 19 April 2022

megathrust earthquakes extending back to 1500C.E have been reconstructed from historical reports of shaking intensity compiled by Silgado (1978) in the work of Dorbath et al. (1990). Notably, the onshore forearc area in southern Peru between Moquegua and Tacna also preserves geomorphological evidence for recent surface-rupturing earthquakes (Benavente et al., 2017; Benavente et al., 2021). It is possible that rupture of these forearc faults may have been misidentified as megathrust earthquakes from the sparse shaking reports in the historical record. Combining the onshore paleoseismic record of forearc earthquakes with the historical record of earthquake shaking provides one way of critically assessing whether historically-reported earthquakes ruptured forearc faults or the megathrust.

In this study, we present new paleoseismological and geomorphological constraints on the size and timing of the last major earthquake along the Purgatorio Fault in the forearc of southern Peru (Fig. 1). We use high-resolution digital elevation models (DEMs) to map the morphology and along-strike distribution of recently-formed fault scarps on the Purgatorio Fault, extending the previous work of Benavente et al. (2017). The scarp mapping enables us to estimate the amount of slip needed to generate the scarps, the total length of the scarps, and therefore magnitude of the most recent surface-rupturing earthquake. We also describe the stratigraphy within a paleoseismic trench excavated across the Purgatorio Fault, and use radiocarbon dating of samples within the trench stratigraphy to place bounds on the timing of the most recent surface-rupturing earthquake. Finally, we compare the timing of this earthquake with the historical record of earthquake shaking along the south Peruvian coastline, and discuss the implications of our findings for seismic hazard assessment in subduction zone settings.

2. Geological setting of the Purgatorio Fault

The Purgatorio Fault is delineated by ~60 km of east-west trending fault scarps in the region between Moquegua and Tacna that were first described by Audin et al. (2006) and Hall et al. (2008) (Fig. 1). The scarps cut across the onshore forearc area of southern Peru, which extends from the magmatic arc of the Western Cordillera to the coastline and is characterised by a gently south-west dipping slope draped in Eocene-Pliocene alluvial gravels and fan surfaces (Roperch et al., 2006). Rivers have incised into the alluvial gravels and the underlying basement of Cenozoic and Mesozoic intrusive, volcaniclastic and sedimentary rock (Roperch et al., 2006), creating a distinctive dendritic drainage pattern in the region (Hall et al., 2008). Fault slip offsets the Plio-Pleistocene alluvial surfaces causing them to become abandoned, uplifts the younger Quaternary alluvium within the active river channels, and deflects the regional drainage pattern (e.g. Benavente et al., 2017).

The scarps along the Purgatorio Fault mostly offset Quaternary

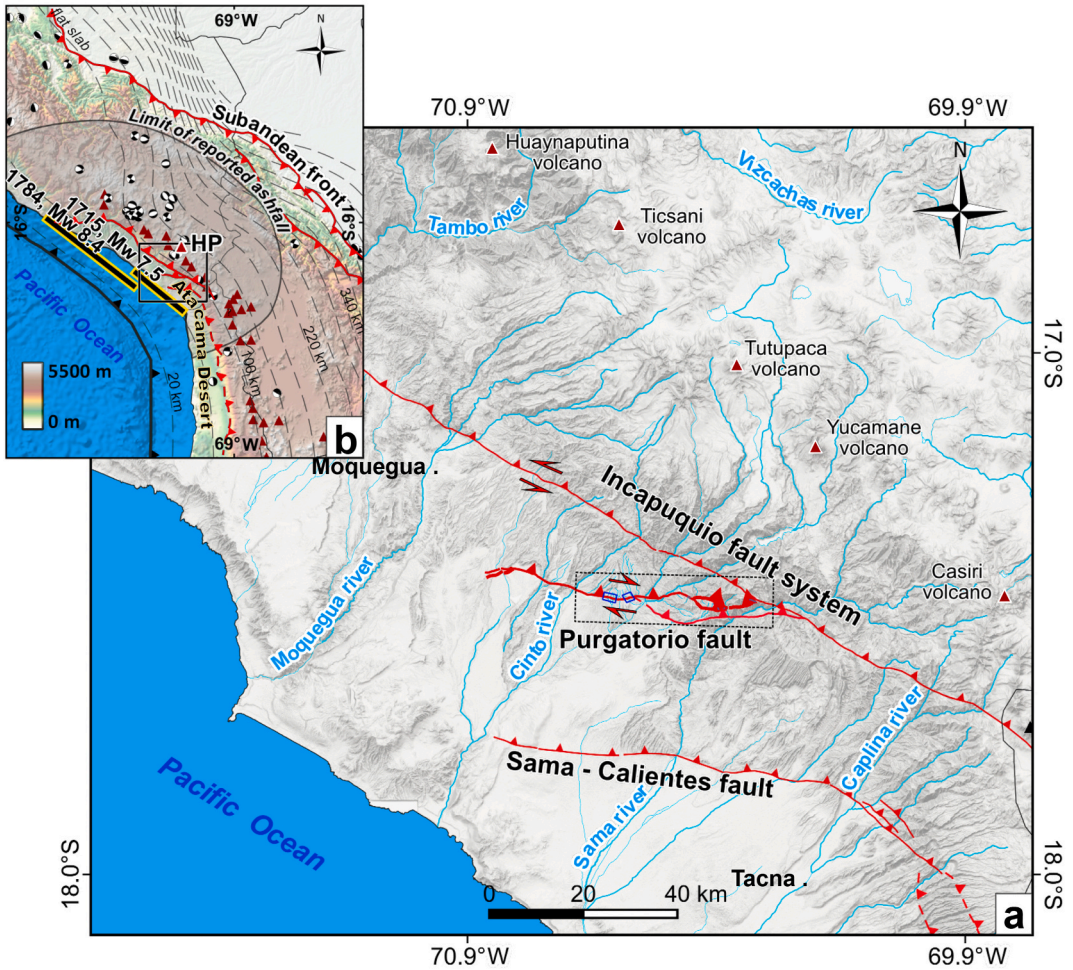

Fig. 1. Overview Map of the Purgatorio Fault and the south Peruvian forearc. (a) Map of the Purgatorio Fault and study area. The black-dashed rectangle indicates the area where we built the high-resolution DEMs using Pleaides satellite imagery. The blue rectangles indicate areas where we constructed high-resolution DEMs using a drone. Blue lines represent rivers. (b) Inset shows the location of the study area in a black rectangle with the approximate boundary of the ash fall recorded in February–March 1600 (Thouret et al., 2002). The black lines indicate the rupture zones of the 1784 and 1715 earthquakes (Dorbath et al., 1990). Black, thin, dashed lines show slab contours from Slab 2.0 (Hayes et al., 2018). Earthquake focal mechanisms are taken from the gCMT catalogue of Ekström et al. (2012). (For interpretation of the references to colour in this figure legend, the reader is referred to the web version of this article.)

alluvial gravels and Eocene-Pliocene Moquegua Group conglomerates along the western section of the fault trace, and cut through the basement of Mesozoic intrusive, volcanoclastic and sedimentary rocks along the eastern section of the fault trace (Fig. 2a-b). Benavente et al. (2017) identified slickenlines on fault scarps within the Moquegua Group deposits between the Cinto river and Ilabaya river (see Fig. 2a), which indicate the Purgatorio Fault accommodated right-lateral transpressional slip in the most recent surface-rupturing earthquake. In addition, by using cosmogenic radionuclide (^{10}Be) exposure dating of quartzite pebbles exposed on a fault plane of a 5 m-high scarp, Benavente et al. (2017) showed that the scarp surface had been exposed sometime during the last 6 kyrs. However, a more detailed chronology of scarp exposure was dependent on estimates of how much ^{10}Be was inherited prior to scarp formation, which remains poorly constrained. As a result, the exact timing and amount of slip in the most recent surface-rupturing earthquake on the Purgatorio Fault remains unknown.

3. Methods

3.1. Fault scarp mapping and morphology

To conduct remote mapping of the Purgatorio Fault scarps we used a combination of optical satellite imagery and high-resolution digital elevation models (DEMs). Preliminary scarp mapping was undertaken using 1 m-resolution optical imagery from Digital Globe (Google Earth) and a 12-m resolution Tandem-X DEM (Rizzoli et al., 2017). For more detailed scarp mapping, and to measure the morphology of the scarps, we subsequently built a 1.3 m-resolution DEM from a stereo pair of Pléiades optical satellite images using NASA's open-source software Ames Stereo Pipeline and the workflow and methodology presented in Lacroix (2016). At two sites along the Purgatorio Fault, we also formed local 10 cm-resolution DEMs derived from low-altitude UAV photogrammetry using the structure-from-motion technique implemented in Agisoft Photoscan (Westoby et al., 2012). When combined, the imagery and DEMs cover an area of ~700 km^2 with high-resolution optical and topographic observations. The DEMs are available through OpenTopography (www.opentopography.org; see Acknowledgments). The fault scarps can be traced within the optical satellite imagery and the DEMs based on a sharp topographic step, shading from topographic slopes and changes in drainage patterns caused by differential uplift either side of the fault.

Laterally-offset river channels across the Purgatorio Fault (Audin et al., 2006; Hall et al., 2008; Benavente et al., 2017) suggest that the slip vector is oblique with a right-lateral component. Therefore, the height of the scarp determined from a topographic profile perpendicular to the fault strike will not always be a good indicator of fault throw and total faut slip needed to form the scarp (see Mackenzie and Elliott, 2017). To accurately calculate the fault throw, a correction to the scarp height measurement must be made. In this correction, the geometric effects of the slope and aspect of the displaced surfaces must be considered, in addition to the dip of the fault and the strike-slip to dip-slip ratio of the fault slip vector (Sl/Sd) (Mackenzie and Elliott, 2017).

An example of the workflow we used to determine the fault throw from the observed scarp heights is shown in Fig. 3. We first calculated the scarp height and its uncertainty using the standard technique of extracting swath profiles through the DEM point clouds perpendicular to the fault strike that follow offset planar and linear features that can be correlated either side of the scarp (Fig. 3a), such as ridge crests, channel thalwegs and fan surfaces (Thompson et al., 2002). The width of the swath profile was ~10 m and was chosen to provide an estimate of the natural variation in the geometry of the planar surfaces above (hangingwall) and below (footwall) the scarp. From the swath profile, we then calculated the slope and aspect of the hangingwall and footwall surfaces, and the vertical offset between the hangingwall and footwall surfaces measured at the center of the fault scarp, using a least-squares routine (Fig. 3b-d). The fault strike, dip and slip vector were determined by using direct measurements of the fault surface, and slickenlines preserved on sections of the fault surface, from nearby exposures (Fig. 3a). From the slickenline data we calculated the strike-slip to dip-slip ratio (Sl/Sd), and apply an uncertainty of 10% on the basis of repeat measurements of the slickenlines. By combining these different measurements, the fault throw can be determined uniquely from the scarp height under the assumption that the surface in the hangingwall and footwall is roughly planar. We then used the Monte-Carlo sampling algorithm of Mackenzie and Elliott (2017) to propagate the uncertainties in each measurement into the uncertainty in fault throw (Fig. 3d). More details on geometrical theory behind the conversion of scarp heights measured by fault-perpendicular profiles into fault throw can be found in Mackenzie and Elliott (2017).

3.2. Paleoseismic trenching

To determine the timing of scarp formation, we excavated a trench perpendicular to the Purgatorio Fault where it offset young alluvial deposits using a back hoe. The trench (17°28′13.10"S/70°34′32.26"W) was ~10 m long, ~3 m deep and ~2 m wide and the northern wall of the trench was excavated, cleaned and logged the northern wall of the trench using the standard method proposed by (McCalpin, 2009). The southern wall of the trench was unstable, as the unconsolidated alluvial gravels repeatedly collapsed covering the outcrop. A number of unique stratigraphic horizons could be recognized within the trench walls on the basis of grain size, colour, clast content and sedimentary structures. We provide a detailed description of each horizon, and their contacts, in Section 4.2.

To place an absolute time-scale on the stratigraphy, we collected a range of different samples for radiocarbon dating. The samples included bulk sediments, large root fragments and small mollusk shells contained within the stratigraphy. Each sample was carefully extracted from the trench wall whilst avoiding contamination, placed inside a foil packet and was dated using Accelerated Mass Spectrometry at the accredited laboratory of Beta Analytic in Miami. All radiocarbon dates were converted into calibrated calendar ages with the program OxCal v4.3.2, which uses a Bayesian statistical method (Bronk Ramsey, 2017) to propagate the analytical uncertainty in the measurement of the ^{14}C:^{13}C ratio, and the uncertainty in the SHCal20 calibration curve (Hogg et al., 2020), through the age calibration.

The different types of samples used for radiocarbon dating will have different relationships with the depositional age of the horizon in which they are contained. Carbonate mollusk shell samples have the simplest relationship with the radiocarbon source and sediment deposition, in that they will date the time at which the animal that made the shell from ingested radiocarbon died and was subsequently buried during deposition of the overlying sediments.

The source(s) of radiocarbon within bulk organic sediment samples can be less clear. The bulk samples were collected from sections of the trench stratigraphy that contained organic plant matter. The plant matter was extracted from the bulk sample and treated using an acid-alkali-acid wash to remove carbonates and secondary organic acids before measuring the radiocarbon content. As a result, the radiocarbon age should reflect the time of death of the plant matter contained within the sediment layer. Comparisons between bulk dating and macro-fossil dating from the same sediment within lake cores indicates that the bulk samples can contain older inherited radiocarbon that biases the radiocarbon ages to be older than the depositional age (e.g. Strunk et al., 2020). We therefore consider the bulk radiocarbon dates to place a lower bound on the layer age.

Roots penetrate below the surface at which the plant was living, and therefore their radiocarbon ages will be younger than the depositional age of the horizon in which they are contained (e.g. Scharer et al., 2011). We carefully selected dead root samples from deep within the trench (0.3–0.8 m below the surface) to avoid the possibility of contamination by any younger rootlets. In addition, given that there is no living

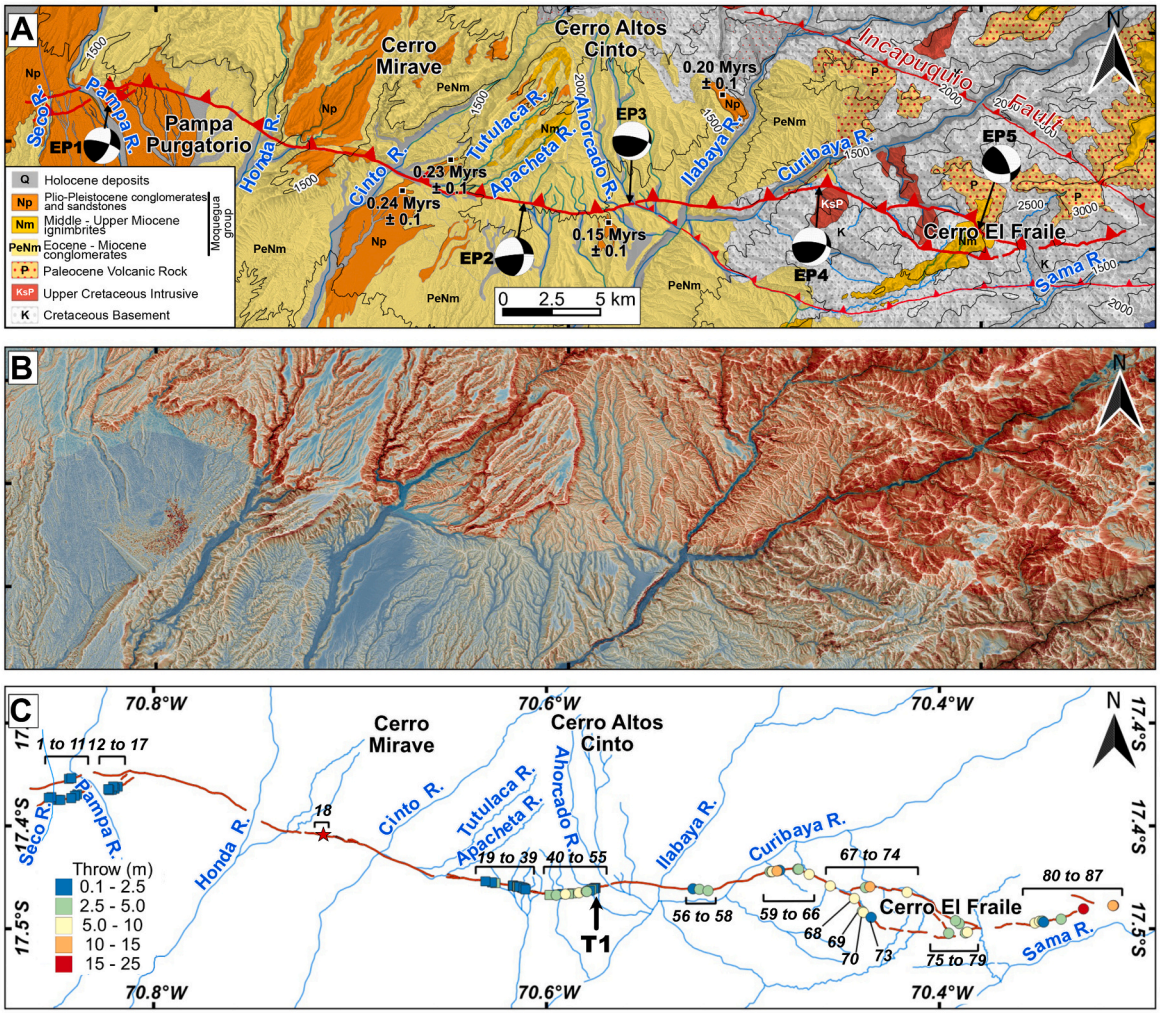

(caption on next page)

Fig. 2. Overview of the fault scarps on the Purgatorio Fault. (a) Geological map of the study area (modified after INGEMMET, 2017). The thin red line represents the active Incapuquio Fault (Benavente et al., 2021), while the thicker red line represents the fault scarp associated with the last rupture of the Purgatorio Fault. EP1, EP2, EP3, EP4 and EP5 are areas where we were able to measure the kinematics of the Purgatorio Fault. The black squares indicate the location of surfaces dated using ^{10}Be and the ages are the mean ages of all the samples with 1σ error (Hall et al., 2008). The thin black lines represent contour lines every 500 m. (b) Topography from a 12 m Tandem-X DEM colored as a Red Relief Image Map (Chiba et al., 2007) highlighting the surface scarps. (c) Scarp height measurements from the 108 fault-perpendicular profiles extracted from the high-resolution DEMs. Topographic profiles measured on Tandem-X are represented by stars, measurements on Pléaides images are represented by circles and measurements on drone images are represented by squares. T1 indicates the location of the palaeoseismological trench. (d-f) Topographic profiles extracted from valley bottoms in the western, central and eastern sector of the Purgatorio Fault, respectively (see location of profiles in Fig. 2c). The profiles show vertical offsets that were then converted into throw following the methodology of Mackenzie and Elliott (2017). USS = Upper Surface Slope and LSS = Lower Surface Slope. (For interpretation of the references to colour in this figure legend, the reader is referred to the web version of this article.)

vegetation visible at the surface at the trench site due to the hyper-aridity of the Atacama Desert, we are confident that the roots we collected from within the trench are not contemporary. We assume the roots post-date the sediment in which they are contained and therefore place an upper bound on the age of the layer from which they were extracted.

4. Results

4.1. Fault scarp observations

In this section, we describe the morphology of the fault scarps along the Purgatorio Fault. At the western end of the fault trace the scarps cut through the Pampa Purgatorio, a ~ 240 ka (Hall et al., 2008) dissected pediment surface that stretches between the Seco river to the Cinto river (Fig. 2a). The fault displaces Pliocene conglomerates and sandstones on the Pampa Purgatorio surface and valley walls, and younger alluvial gravels within the river valleys (Fig. 2a). We mapped three strands of fault scarps on the Pampa Purgatorio and extracted seventeen topographic profiles across these scarps from the high-resolution DEMs (see Supporting Information S1). The topographic profiles were measured on the floor of the valleys where the fault cuts recent alluvial deposits and vary between 0.4 ± 0.1 m and 1.5 ± 0.1 m (Fig. 2c and d).

Within the banks of the Pampa river, the Purgatorio Fault plane is well exposed offsetting a ~10 m-thick succession of Pliocene-Pleistocene conglomerates and sandstones (Fig. 4a-b). Slickenline measurements from this fault plane at site EP1 show a strike of N270–315°, dip angle 65–85° and a slip vector pitching 20–45° towards the southeast (see Supporting Information S2). At the top of the stratigraphy, we identified a ~0.3 m-thick ash horizon that is folded in a reverse sense (Fig. 4a-b). The ash layer is covered by ~1 m of alluvial gravel, forming an angular unconformity. A similar stratigraphic sequence was described by Magilligan et al. (2008) in the lower terrace along the banks of the Moquegua river ~25 km west of the Pampa Purgatorio. Magilligan et al. (2008) correlated the ash layer with the widespread ashfall associated with the eruption of Huaynaputina in 1600C.E, which covered most of southern Peru and northern Chile (Thouret et al., 1999), on the basis of optically-stimulated luminescence exposure dating and radiocarbon dating of units above and below the layer. The deposit described in Magilligan et al. (2008) and the ash deposit at the Rio Pampa are located within the same isopach from the eruption (Prival et al., 2019). The ash layer thickness and isopach overlap suggest that these ash deposits are correlated, which is further supported by the comparable stratigraphy observed in the banks of the Rio Pampa and the Rio Moquegua. If the ash layer we identified in the banks of the Pampa Purgatorio does date from the eruption of Huaynaputina, then it suggests the unit was offset by slip on the Purgatorio Fault at some point in the last 400 years.

The center of the fault trace between the Cinto river and Curibaya river consists of near-continuous fault scarps that cut through southward-draining river valleys and their intervening ridges. The ridges are typically formed of Eocene-Miocene conglomerates of the Moquegua Group, while in the river valleys the conglomerates are covered by young alluvial deposits (Fig. 4c). We extracted forty-one topographic profiles perpendicular to the fault scarps from the high-resolution DEMs in this area (Fig. 2c). Eighteen of the topographic profiles were measured in the valley floors where the fault cuts through young alluvial deposits (Fig. 5), which had scarp heights ranging from 0.5 ± 0.1 m and 3.8 ± 0.1 m. The other twenty-three profiles were measured on the crests and slopes of ridges outside of the river valleys (Fig. 4c). These scarp heights range between 0.2 ± 0.1 m and 13.3 ± 1.4 m (Fig. 2c and e). Exposures of the Purgatorio Fault surface are abundant between the Cinto river and Curibaya river, and often contain fractured clasts with slickenlines (Fig. 4d). At site EP2 the fault plane had strike of N257°-270°, dip angle 75°-85° and contained slickenlines pitching 32°-50° towards the east (Fig. 4c). At site EP3 the fault plane had a strike of N280°-285° and dip angle 70°-75° and contained slickenlines pitching 55°-80° towards the south (Fig. 4d).

Along the eastern-most section of the Purgatorio Fault the fault scarps cut older Mesozoic volcaniclastic and sedimentary rocks, Cenozoic intrusive rocks, and young alluvial deposits within river valleys (Fig. 4e). This section of the fault displays evidence of right-lateral offsets along the crests of ridges, streams and terrace risers of 2–4 m (Fig. 4f and 2f). We extracted twenty-eight topographic profiles perpendicular to the fault scarps from the DEMs in this region. Four of the profiles were measured on fault scarps that offset young alluvial deposits (Fig. 5), which yield scarp heights between 1.8 m ± 0.5 m and 5.4 ± 0.5 m. The other twenty-nine topographic profiles were measured across bedrock scarps and offset ridge lines and recorded scarp heights between 0.5 m ± 0.1 m and 16.1 ± 4.9 m.

We were able to collect slickenline measurements at two positions along the eastern section of the fault. At EP4 the fault plane had strike of N260°-288°, dip angle of 65°-75° with the slickenlines pitching N55°-69° towards the southeast (Fig. 3e). At EP5 the fault had strike of N297°-356°, dip angle 50°-84° and contained slickenlines pitching 26°-57° towards the south (Fig. 4f).

The measured scarp heights vary significantly along the length of the Purgatorio Fault. Some component of the scarp height variability may be related to the effects landform geometry. To account for this, we converted the scarp heights into fault throw using the measurements of fault dip, fault slip vector and landscape geometry using the method described in Section 3.1 (Fig. 5). We find that the effect of landscape geometry means that the scarp heights approximate the throw to within ~10–20% of the scarp height, as most of the offset surfaces have shallow dips and the Purgatorio Fault has a steep dip. The mean fault throw in the full set of measurements is 1.4 ± 0.1 m (2σ uncertainty) with most fault throw estimates clustering between 1 m and 3 m (Fig. 5).

Some component of variability in the scarp heights is also related to the offset of different age horizons (Fig. 5), with the smallest scarp heights being preserved within alluvial sediments recently deposited in river channels and the largest scarps being preserved along the intervening ridge crests and fan surfaces (see Fig. 5). Almost all of the scarps preserved within or along the margins of river channels are between 1 m and 3 m high. In the following section, we use paleoseismic trenching across one of these scarps preserved in young alluvial deposits to determine its timing of formation.

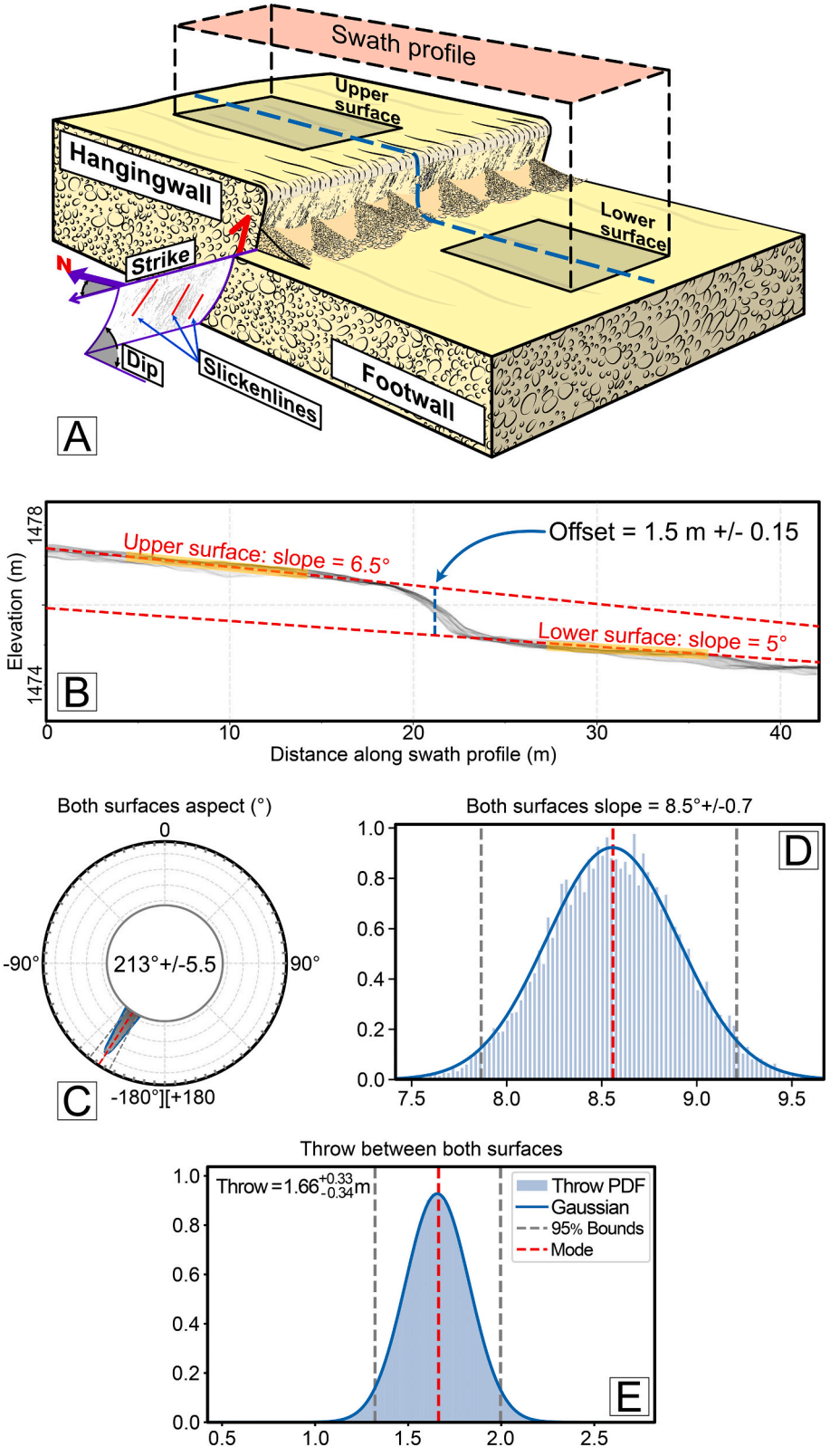

Fig. 3. (a) Sketch showing the measurements and workflow used for calculating the fault throw from a fault scarp. The pink rectangle represents a swath profile acquired perpendicular to the fault scarp. Rectangles with black borders represent surfaces that were continuous prior to fault activity. (b) Two-dimensional analysis for calculating the vertical separation between the hangingwall and footwall surfaces at the point approximately in the center of the scarp. (c) 3D analysis of the aspect of the hangingwall and footwall surfaces. (d) Analysis of the dip of both surfaces. (e) Calculation of the fault throw from the vertical offset in (b) and the slope geometry in (c,d) using the method of Mackenzie and Elliott (2017). (For interpretation of the references to colour in this figure legend, the reader is referred to the web version of this article.)

4.2. Paleoseismology on the Purgatorio Fault

We identified a site for paleoseismic trenching where the Purgatorio Fault offsets the bedload of the Ahorcado river forming an scarp varying from 2.0 to 1.5 m in height. Rock outcrop adjacent to the Ahorcado river valley consists of the Eocene-Miocene conglomerates of the Moquegua Group, whilst the floor of the river valley is formed by young alluvial gravels that have been deposited in the channel of the ephemeral Ahorcado river (INGEMMET, 2017).

The trench (T1) is located at 17°28′13.10”S/70°34′32.26”W and is 10 m-long, 3 m-deep and 2-m wide. Within the trench walls we identified a steeply dipping fault (F1) with orientation N258°/70° that cuts

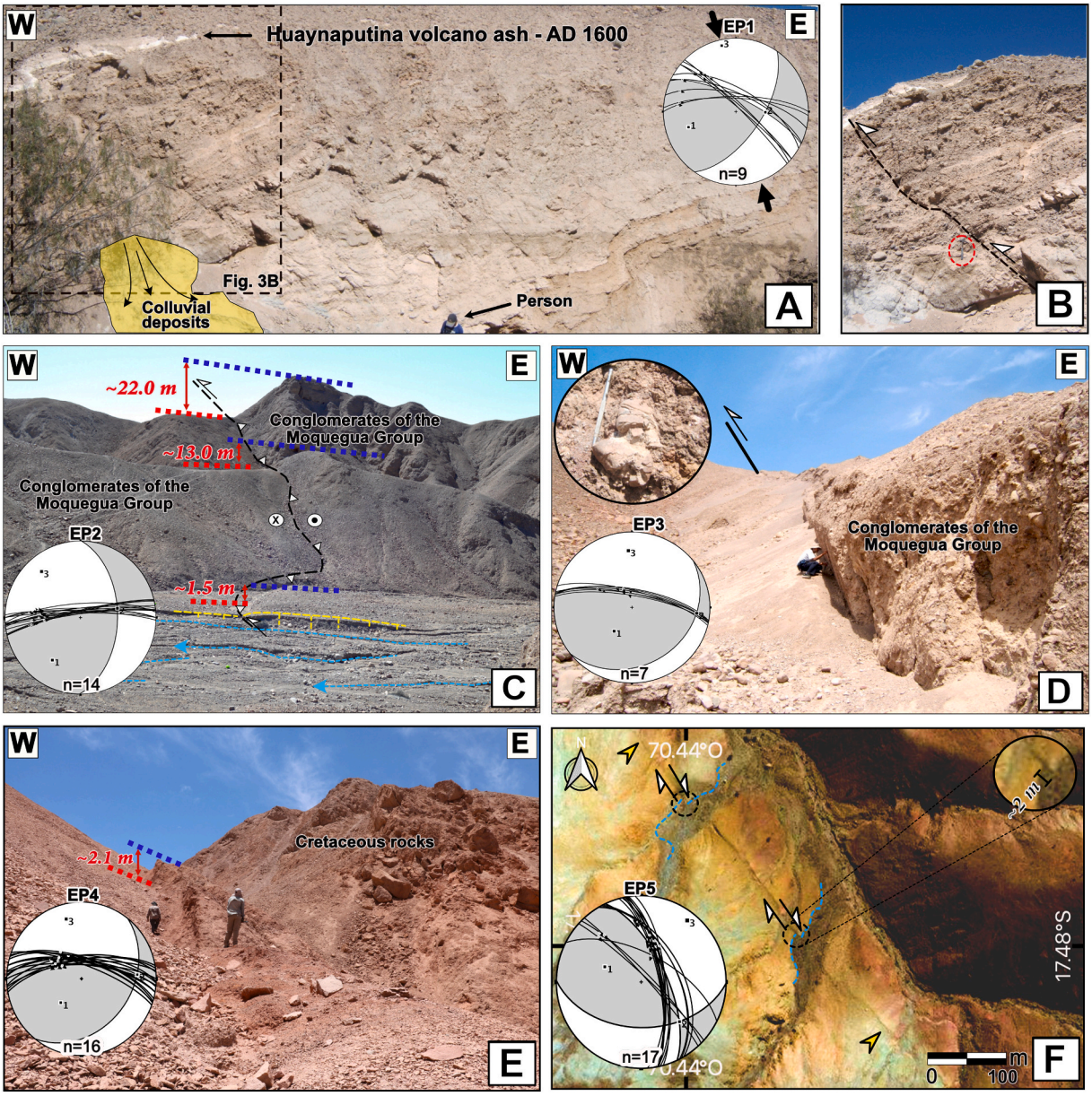

Fig. 4. Field photographs of scarps on the Purgatorio Fault. (a) Natural exposure of the Purgatorio Fault in the banks of the Pampa river, where folded alluvial and ash deposits are exposed. A lower hemisphere projection of the fault plane and slickenlines is shown inset (produced using FaultKinWin® by Allmendinger (2001)). The yellow polygon with black border represents colluvial deposits that fell from the hillside, covering part of the outcrop. Note at the bottom a person as a scale. (b) Detailed view of the Purgatorio Fault showing the deposits deformed by the reverse movement. The black dashed line shows the fault trace. The red circle indicates a geologist's hammer for scale. (c) Purgatorio Fault cutting conglomerates of the Miocene Moquegua Formation, as well as recent alluvial deposits along the fluvial valleys. Vertical displacements vary from 1.5 m to 22 m in the field of view, demonstrating the along-strike variability in the scarp heights; dashed lines are linear fits to the slopes above (blue) and below (red) the scarp. (d) Bedrock scarp on the Purgatorio Fault where rocks of the Moquegua formation are exposed. Clasts in the Moquegua conglomerates were fractured and contain slickenlines. The bedrock scarp is ~1.5 m high. (e) Well-preserved fault scarp (~2.1 m high) that dips steeply towards the north and displaces Cretaceous rocks against recent alluvial deposits. (f) Trace of the Purgatorio fault cutting alluvial deposits and where lateral displacement of up to ~2 m can be observed. Location of photographs in Fig. 2B. (For interpretation of the references to colour in this figure legend, the reader is referred to the web version of this article.)

through consolidated rocks of the Moquegua Group and younger alluvial deposits (Fig. 5b). The trench wall also contains nine distinct stratigraphic units above the Moquegua Group conglomerates that can be recognized on the basis of their grain size, clast content, coloration and sedimentary structures, which we term units U1 (older) to U8 (younger) (Fig. 5c). Four of these units (U1-U4) can be correlated between the hangingwall and footwall of the trench. Below we give a brief description of these units, their relative ages, and the radiocarbon dating constraints on their depositional ages.

The base of the trench is formed of consolidated conglomerates of the Moquegua Group, which have a sharp erosional contact with the overlying and less-consolidated alluvial gravels of units U1-U7 (Fig. 5c). Where the fault scarp cuts through the trench, the Moquegua Group rocks are displaced vertically in a reverse sense by 1.5 m with north-up kinematics. The vertical offset of the top of the Moquegua Group is similar to the 1.6 m height of the fault scarp measured at the surface (Fig. 2a). Unit U1 directly overlies the Moquegua Group in both the footwall and hangingwall and consists of a 0.2–0.3 m-thick layer of rounded to subrounded, poorly-sorted cobble and pebble-sized clasts in a sand-silt matrix. U1 is then overlain by a series of gently south-dipping,

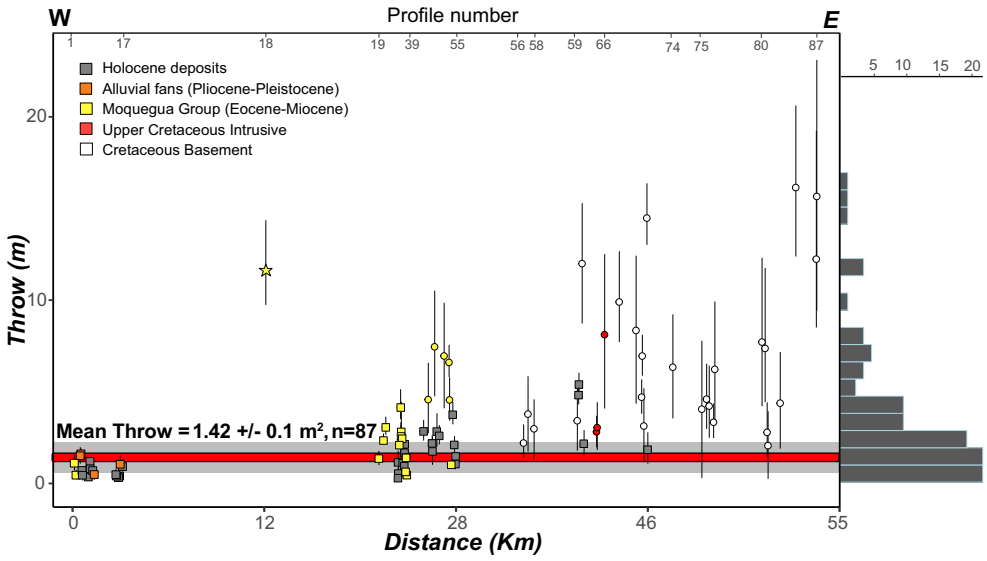

Fig. 5. Compilation of throw measurements with their respective uncertainty along the Purgatorio fault. For some of the sites, the percentage uncertainty is smaller than the size of the symbol. Squares represent measurements taken from DEMs constructed using drones, the circles are from Pléiades satellite imagery, and the stars from Tandem-X imagery. The measurements are represented with different colours according to the lithology where the Throw was calculated (see Fig. 2a). The red line represents mean scarp height of 1.4 ± 0.1 m, and the light-gray band is the 1-sigma standard deviation. The dark-gray band is the standard error in the estimate of the mean (0.1 m). A histogram of the scarp heights is shown by the gray bars on the right binned in 0.4-m intervals. There is a clear cluster of scarp heights between 0.5 and 3 m. The numbers at the top indicate the profile number and are according to the intervals in Fig. 2c. (For interpretation of the references to colour in this figure legend, the reader is referred to the web version of this article.)

sub-parallel units of alluvial gravels (U2-U4) that can be distinguished based on their clast and matrix content. Unit U2 consists of a massive, clast-supported gravel with mud-to-sand sized matrix and with flat or random clast orientations. Unit U3 consists of a pebble-sand matrix supported gravel with random clast orientation. Unit U4 consists of massive, clast-supported gravel with a muddy, sandy matrix and parallel clast alignment. U5-U7 outcrop only on the fault footwall and are composed of pebble-sized boulders and clasts in a sandy matrix. U6 differs from U5 and U7 in that it is poorly sorted and has clasts with diameters varying between 0.01 and 0.2 m (See Supporting Information S3).

Two mollusk shell samples collected from unit U1 in the footwall and unit U3 in the hangingwall yielded radiocarbon dates of 15,191–14,690 B.C.E (GA50B-P8) and 13,866–13,450 B.C.E (GA50B-P6), respectively (Supporting Information S4). A dead root sample collected from the top of unit U6 yielded two main radiocarbon date ranges of 1622–1676C.E (58.4% probability) and 1736–1799C.E (24.8% probability). The two date populations for this root sample are a result of the plateau within the SHCal13 calibration curve between 1650C.E and 1800C.E. We assume that the time of death of the organisms that created these samples can be used to approximately date the timing of deposition of the units in which they are contained.

Units U1-U7 abut sharply against a triangular wedge (W1) of deformed alluvial material and the uplifted Moquegua Group conglomerates, but show no sign of thickening towards or away from fault F1 (Fig. 6). Adjacent to contemporary bedrock scarps exposed at the surface along the Purgatorio Fault, the footwall is always draped in a talus slope of loose, gravelly material that dips away from the scarp (e.g. Fig. 3d). Therefore, the sub-horizontal dip of units U1-U7 supports the view that they were deposited prior to faulting, and therefore the radiocarbon dating of these layers indicates that the most recent surface-rupturing earthquake occurred after 1622–1676C.E. (See Fig. 6c)

The ages of U1 and U3 correlate with one of the major expansions of the Altiplano lakes, specifically the Tauca phase (16,500–13,500 B.C.E) during the Heinrich Stadial 1a (Placzek et al., 2013). Units U1-U3 could have formed as a result of sediment accumulation within the Ahorcado river valley during this particularly 'wet' period (Fig. 5d), which has been reported by Steffen et al. (2009) in valleys located ~250 km to the northwest of the trench location, as well as in valleys located in northern Chile (Riquelme et al., 2011). The time gap between the deposition of U1-U3 and U6 suggests that parts of the river bed can go through long periods with little, or no, deposition, which most likely occur during particularly dry periods where there is no bedload transport in the Ahorcado river.

In the center of the trench, units U1-U7 and fault F1 are capped by an angular unconformity, above which is a chaotic deposit with no recognizable internal grading or layering, which we term unit W1. Unit W1 is not offset by fault F1, suggesting it post-dates the faulting that offset units U1-U7. W1 is also thickest in the footwall immediately adjacent the fault, which is a typical feature of colluvial wedge deposits (e.g. Deng and Zhang, 2000; McCalpin, 2009). Further into the footwall, W1 is itself overlain by another unit (U8). Unit U8 has an angular unconformable contact with U1-U7 and W1, suggesting it post-dates these units.

We collected two dead root fragments from the base of U8 (Fig. 5c) at sites located 0.3 m and 0.8 m below the dry soil at the surface. Despite the lack of vegetation on the contemporary surface, root fragments within the sub-surface are relatively common in the Atacama Desert and are thought to reflect periods of vegetation growth during wetter climatic conditions in the past (Ewing et al., 2008). We are therefore confident that the roots we collected from U8 are not contemporaneous with the surface, but the roots may well be younger than the stratigraphic horizon in which they sit. AMS dating yielded radiocarbon ages of 1668–1787C.E (46.6% probability) and 1826–1894C.E (25.2% probability) for the root samples. The bi-modality of the probability density functions of the sample ages results from plateau in the SHCal13 calibration curve over this particular time period, as well as different possible sources of radiocarbon within the sample. Nonetheless, these sample ages still place a lower bound on the age of unit U8, which we interpret to have post-dated the most recent surface-rupturing earthquake given that it overlies layers that are not offset across the fault. Notably, these root ages correlate with the great Chuza flood event (Fig. 5d), consisting of widespread debris flows overlying the Huaynaputina ashes (1600 C.E) dated between 1636 and 1804 C.E by Zaro et al. (2013) and Magilligan et al. (2008).

Given that the trench preserves sediments that pre- and post-date scarp formation, and these layers have a clear stratigraphic order, we have used the methodology proposed by Lienkaemper and Ramsey (2009) to build an OxCal stratigraphic model (Bronk Ramsey, 2009) to estimate the most probable timing of the scarp-forming event. The OxCal method uses Bayesian statistics to combine the probability density functions of each sample's radiocarbon date, as well as stratigraphic constraints on the relative ages of these samples, to estimate the

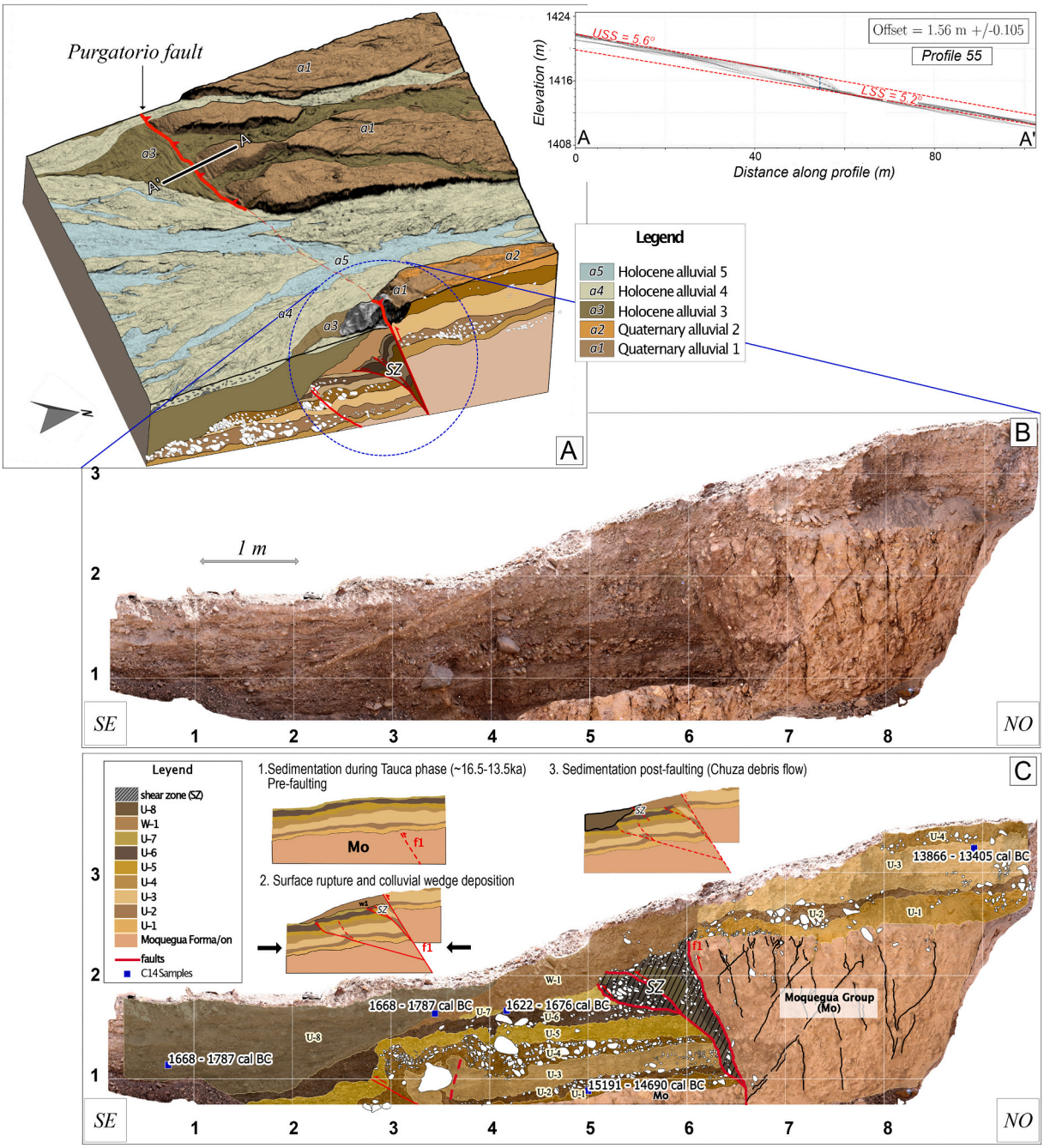

Fig. 6. Morphology and stratigraphy of trench T1 at Ahorcado. (a) Oblique aerial view of the trench location relative to the topography (derived from a high-resolution drone DEM) and surface deposits within the Ahorcado river bed. The trench is located along the margins of an active river channel. The red line and triangles represent the Purgatorio Fault. The black line with white border represents the topographic profile A-A' adjacent to the palaeoseismological trench showing a vertical offset of 1.6 m. (b) Photomosaic of the west wall of the trench. (c) Interpretation of the stratigraphy in the trench. Radiocarbon ages are shown by blue squares. Variations in clast content is shown by white polygons, and the location of the deformed zone (shear zone) near the fault surface is shown with black hachuring. A schematic interpretation of how the trench stratigraphy formed between 16 ka to the present day. (For interpretation of the references to colour in this figure legend, the reader is referred to the web version of this article.)

probability density function of the timing of the scarp-forming earthquake. The results of the analysis are shown in Fig. 7. Given that the timing of the faulting is between the ages of units U6 and U8, we find that fault slip most likely occurred sometime between 1630C.E and 1790C.E (Fig. 7).

5. Discussion

5.1. Paleoearthquake magnitude and timing

The cumulative length of the mapped fault scarps along the Purgatorio Fault is 60 ± 5 km, stretching from the Pampa Purgatorio in the west to the Incapuquio Fault in the east. The fault throw needed to form the scarps varies significantly along-strike (Fig. 2c). Nonetheless, where the scarps cut young alluvial deposits, they range only between 1 m and

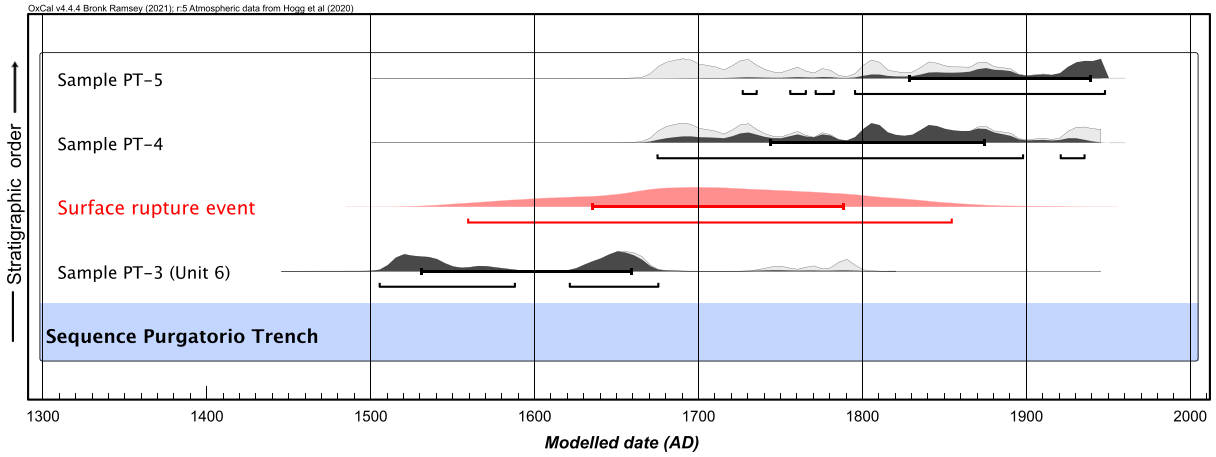

Fig. 7. OxCal chronostratigraphic model for the most recent surface-rupturing earthquake recorded in the palaeoseismological trench at Ahorcado. Light gray probability density functions (PDFs) show the likelihood distributions of the radiocarbon measurements for the samples that bracket the timing of faulting. Dark gray PDFs are the modelled (i.e. posterior) PDFs. Bars beneath the PDFs are the 68th (i.e. 1-sigma) and 95th (i.e. 2-sigma) percentile range. The red PDF shows the possible timing of the surface-rupture formation, which has a 1-sigma range between 1630 and 1790 CE. (For interpretation of the references to colour in this figure legend, the reader is referred to the web version of this article.)

3 m high (see gray-outlined points on Fig. 5). We interpret these smallest and youngest scarps to have been formed in the most recent surface-rupturing earthquake on the Purgatorio Fault given the evidence for only 1 large earthquake in the trench T1, with the taller scarps representing cumulative offsets from multiple events.

In order to estimate the net surface slip in the most recent surface-rupturing earthquake on the Purgatorio Fault, we focus on three localities where both the scarp is well preserved and we have good estimates of the fault slip vector. The first locality is in banks of the Pampa river (Fig. 3a) where a folded ash layer thought to date from the 1600C.E eruption of Huaynaputina (Thouret et al., 2002) is vertically displaced by 0.5 m along a plane dipping at 75° that contains slickenlines pitching 33°, giving a total fault slip of 2.1 m. The second locality is the palaeoseismic trench T1, where the Moquegua Formation is vertically displaced by 1.6 m with a mean fault dip of 80° and slickenlines pitching of 41°, yielding a fault slip of 2.2 m. The third locality is located 1 km east of trench T1, where we calculated the height of the bedrock fault scarp (Fig. 3d) to be 1.7 m, and the fault is well exposed having a mean dip of 80° and slickenlines pitching of 41°, yielding a fault slip of 2.4 m.

The estimated slip is similar to the average scarp heights found from the topographic profiles, which is expected given the steep fault dip is steep (Fig. 4). Using a fault slip of 2.1–2.4 m suggests the ratio of fault slip to length is 2–3 $\times$ 10^{-5}, which is typical for intraplate earthquakes (Scholz, 1994). The estimated moment magnitude of the last scarp-forming earthquake using 2.2 m of net slip on a 60 km long fault is M_w 7.0 and M_w 7.2 according to the empirical scaling laws of Wells and Coppersmith (1994) and Stirling et al. (2013), respectively. Statistical spread in these scaling laws will lead to at least a further uncertainty of ~0.1 magnitude units on these estimates (i.e. M_w 6.9–7.3).

5.2. Comparison between the paleoseismic and historical record

The results of the paleoseismic trenching and the geomorphological analysis indicate that most recent scarp-forming earthquake occurred sometime during 1630–1790C.E, generating a ~ 2 m-high surface rupture from a Mw 6.9–7.3 earthquake. A shallow earthquake of this size will have caused notable surface shaking in the region, and therefore is likely reported in the written historical record of seismicity in Peru, which begins with the records of Spanish colonialists in the 16th century.

Compilations of historical seismicity in Peru have been produced by Silgado (1978), and updated more recently by Dorbath et al. (1990). The records are mainly based on the reports of colonial settlers and European travelers in South America. Two major earthquakes have been reported in southern Peru during the period 1630–1790C.E. The largest earthquake was reported in 1784C.E. Barriga (1951) and Polo (1899) describe the tsunami that resulted from this event, and large cracks that formed along the coast of Arequipa and Moquegua, as well as fallen houses and churches in Arequipa. Large cracks along the coastline were also widely observed following the 2001 Mw 8.4 Arequipa earthquake (Keefer and Moseley, 2004), and are thought to reflect permanent deformation of the forearc following coseismic extension (e.g. Baker et al., 2013). Given the similarities between the 1784C.E and 2001C.E earthquakes, as well as the reports of a tsunami along the coastline, it is most likely that the 1784C.E earthquake ruptured the megathrust offshore and not the Purgatorio Fault (Dorbath et al., 1990).

The second event in the historical record occurred in 1715C.E and was reported by Le Barbinais Le Gentil (1728), a French traveler who had arrived at the port of Arica at the beginning of July 1715. Le Gentil's account describes a large earthquake that mainly affected the regions of Arica, Tacna, Moquegua, and, to a lesser extent, the city of Arequipa. He also reports that the 1715C.E earthquake led to significant damage to settlements in the high Andes, with landslides burying villages (Le Barbinais Le Gentil, 1728). The geographic distribution of the damage led Lomnitz (1970) to catalogue this earthquake as a magnitude M 7.5 event that ruptured the megathrust somewhere between Moquegua and Arica. Dorbath et al. (1990) inferred a rupture length on the order of 50 to 100 km, but noted that this earthquake is not particularly well documented and is based on a single account.

Based on the historical report, and our new radiocarbon-dating constraints on scarp formation, it is possible that the 1715C.E earthquake was in fact generated by rupture of the Purgatorio Fault. The 1715C.E event was previously inferred to have ruptured the megathrust offshore (e.g. Villegas-Lanza et al., 2016). However, the damage distribution, estimated magnitude, timing and location of the 1715C.E earthquake are all consistent with a rupture on the Purgatorio Fault. A more quantitative comparison is limited by the lack of detailed damage reports or shaking intensities from the historical record. Nonetheless, our paleoseismological results highlight the possibility that faulting within the forearc can generate large earthquakes, therefore must be considered as possible sources of shaking when analyzing the historical record within subduction zones, particularly for events estimated to be M ~ 7. The Purgatorio Fault is one of many faults related to the Incapuquio Fault System that show geomorphic evidence of Holocene activity (Audin et al., 2006; Benavente and Audin, 2009; Benavente et al., 2017, 2021; Hall et al., 2008, 2012; Macharé et al., 2009). These faults

should be considered as potential hosts for historical and future seismicity, particularly given that the ground motions associated with earthquakes on shallow, onshore faults can pose an acute hazard to infrastructure and population centers within the Andean forearc and the coastline of South America.

6. Conclusions

We mapped 60 km of fault scarps along the Purgatorio Fault in the forearc of southern Peru. The heights of the fault scarps vary between 1 m and 17 m along-strike, but where they cut young alluvial deposits within river valleys the scarp heights are clustered between 1 m and 3 m. Converting the scarp heights into net fault slip using measurements of the fault geometry and slip vector indicates that the slip required to form the fault scarps is 2.1–2.4 m. Our trench chronology brackets the age of the scarp formation to be 1630–1790C.E. We suggest that the scarps may have been formed by a M_w 7 earthquake reported in the historical catalogue in 1715C.E, which was previously attributed to an earthquake that ruptured the megathrust. We argue that forearc faults in southern Peru are potential sources of historical and future earthquakes, and therefore should be considered in seismic hazard estimates and mechanical models of deformation of the forearc.

Declaration of Competing Interest

The authors declare that they have no known competing financial interests or personal relationships that could have appeared to influence the work reported in this paper.

Acknowledgments

This work is part of INGEMMET's research and was funded through the GA-50 project "Neotectonic Studies in Peru". SW was supported by the Denman Baynes Junior Research Fellowship at Clare College, Cambridge. Supplementary information contains topographic profile figures across the fault scarp, structural data, detail of the palaeoseismological trench stratigraphy and radiocarbon ages. The drone DEMs are freely available through OpenTopography (www.opentopography.org) at https://doi.org/10.5069/G9DV1H36.

Appendix A. Supplementary data

Supplementary data to this article can be found online at https://doi.org/10.1016/j.tecto.2022.229355.

References

Audin, L., David, C., Hall, S., Farber, D., Hérail, G., 2006. Geomorphic evidences of recent tectonic activity in the forearc, southern Peru. Rev. Asoc. Geol. Argent. 61, 545–554.
Baker, A., Allmendinger, R.W., Owen, L.A., Rech, J.A., 2013. Permanent deformation caused by subduction earthquakes in northern Chile. Nat. Geosci. 6, 492–496.
Barriga, V.M., 1951. Los terremotos en Arequipa, 1582–1868: Documentos de los archivos de Arequipa y de Sevilla. La Colmena.
Benavente, C., Audin, L., 2009. Geometría, morfología y peligro sísmico de la falla Purgatorio Mirave-Antearco del sur del Perú. Bol. Soc. Geol. Perú 103, 15–26.
Benavente, Carlos, Swann, Zerathe, Laurence, Audin, Hall Sarah, R., Xavier, Robert, Fabrizio, Delgado, Julien, Carcaillet, Team ASTER, 2017. Active transpressional tectonics in the Andean forearc of southern Peru quantified by 10Be surface exposure dating of an active fault scarp. Tectonics 36, 1662–1678.
Benavente, C., Wimpenny, S., Rosell, L., Robert, X., Palomino, A., Audin, L., Aguirre, E., García, B., 2021. Paleoseismic evidence of an Mw 7 Pre-Hispanic earthquake in the Peruvian Forearc. Tectonics 40, e2020TC006479.
Bronk Ramsey, C.B., 2009. Bayesian analysis of radiocarbon dates. Radiocarbon 51, 337–360.
Bronk Ramsey, C.B., 2017. Methods for summarizing radiocarbon datasets. Radiocarbon 59, 1809–1833.
Chiba, T., Suzuki, Y., Hiramatsu, T., 2007. Digital terrain representation methods and red relief image map, a new visualization approach. Map J. Jpn. Cartogr. Assoc. 45, 27–36.
Deng, Q., Zhang, P., 2000. Colluvial wedges associated with pre-historical reverse faulting paleoearthquakes. Chin. Sci. Bull. 45, 1598–1604.
Dorbath, L., Cisternas, A., Dorbath, C., 1990. Assessment of the size of large and great historical earthquakes in Peru. Bull. Seismol. Soc. Am. 80, 551–576.
Ekström, G., Nettles, M., Dziewoński, A.M., 2012. The global CMT project 2004–2010: Centroid-moment tensors for 13,017 earthquakes. Phys. Earth Planet. Inter. 200–201, 1–9.
Ewing, S., Macalady, J., Warren-Rhodes, K., McKay, C., Amundson, R., 2008. Changes in the Soil C Cycle at the Arid-Hyperarid Transition in the Atacama Desert. https://doi.org/10.1029/2007JG000495.
Hall, S.R., Farber, D.L., Audin, L., Finkel, R.C., Mériaux, A.-S., 2008. Geochronology of pediment surfaces in southern Peru: implications for Quaternary deformation of the Andean forearc. Tectonophys. New Insights Andean Evol. 459, 186–205.
Hall, S.R., Farber, D.L., Audin, L., Finkel, R.C., 2012. Recently active contractile deformation in the forearc of southern Peru. Earth Planet. Sci. Lett. 337–338, 85–92.
Hayes, G.P., Moore, G.L., Portner, D.E., Hearne, M., Flamme, H., Furtney, M., Smoczyk, G.M., 2018. Slab2, a comprehensive subduction zone geometry model. Science 362, 58–61.
Hogg, A.G., Heaton, T.J., Hua, Q., Palmer, J.G., Turney, C.S., Southon, J., Bayliss, A., Blackwell, P.G., Boswijk, G., Ramsey, C.B., Pearson, C., Petchey, F., Reimer, P., Reimer, R., Wacker, L., 2020. SHCal20 Southern Hemisphere Calibration, 0–55,000 years cal BP. Radiocarbon 62, 759–778. https://doi.org/10.1017/RDC.2020.59.
Keefer, D.K., Moseley, M.E., 2004. Southern Peru desert shattered by the great 2001 earthquake: Implications for paleoseismic and paleo-El Niño–Southern Oscillation records. Proc. Natl. Acad. Sci. 101, 10878–10883.
Lacroix, P., 2016. Landslides triggered by the Gorkha earthquake in the Langtang valley, volumes and initiation processes. Earth Planets Space 68, 46.
Le Barbinais Le Gentil, 1728. Voyage Autour du Monde, Paris.
Lienkaemper, J.J., Ramsey, C.B., 2009. OxCal: versatile tool for developing paleoearthquake chronologies – a primer. Seismol. Res. Lett. 80, 431–434.
Lomnitz, C., 1970. Major earthquakes and tsunamis in Chile during the period 1535 to 1955. Geol. Rundsch. 59, 938–960.
Macharé, J., Benavente Escobar, B., Audin, L., 2009. Síntesis descriptiva del mapa neotectónico 2008 - [Boletín C 40].
Mackenzie, D., Elliott, A., 2017. Untangling tectonic slip from the potentially misleading effects of landform geometry. Geosphere 13, 1310–1328.
Magilligan, F.J., Goldstein, P.S., Fisher, G.B., Bostick, B.C., Manners, R.B., 2008. Late Quaternary hydroclimatology of a hyper-arid Andean watershed: climate change, floods, and hydrologic responses to the El Niño-Southern Oscillation in the Atacama Desert. Geomorphology. In: The 39th Annual Binghamton Geomorphology Symposium: Fluvial Deposits and Environmental History: Geoarchaeology, Paleohydrology, and Adjustment to Environmental Change, vol. 101, pp. 14–32.
McCalpin, J.P., 2009. Paleoseismology. Academic Press.
Placzek, C.J., Quade, J., Patchett, P.J., 2013. A 130ka reconstruction of rainfall on the Bolivian Altiplano. Earth Planet. Sci. Lett. 363, 97–108.
Polo, J.T., 1899. Sinopsis de temblores y volcanes del Perú; siglos XVI-XIX. Bol. Ciedad Geogr. Lima 8, 7.
Pritchard, M.E., Norabuena, E.O., Ji, C., Boroschek, R., Comte, D., Simons, M., Dixon, T. H., Rosen, P.A., 2007. Geodetic, teleseismic, and strong motion constraints on slip from recent southern Peru subduction zone earthquakes. J. Geophys. Res. Solid Earth 112.
Prival, J.-M., Thouret, J.-C., Japura, S., Gurioli, L., Bonadonna, C., Mariño, J., Cueva, K., 2019. New insights into eruption source parameters of the 1600 CE Huaynaputina Plinian eruption, Peru. Bull. Volcanol. 82, 7. https://doi.org/10.1007/s00445-019-1340-7.
Riquelme, R., Rojas, C., Aguilar, G., Flores, P., 2011. Late Pleistocene–early Holocene paraglacial and fluvial sediment history in the Turbio valley, semiarid Chilean Andes. Quat. Res. 75, 166–175. https://doi.org/10.1016/j.yqres.2010.10.001.
Rizzoli, P., Martone, M., Gonzalez, C., Wecklich, C., Borla Tridon, D., Bräutigam, B., Bachmann, M., Schulze, D., Fritz, T., Huber, M., Wessel, B., Krieger, G., Zink, M., Moreira, A., 2017. Generation and performance assessment of the global TanDEM-X digital elevation model. ISPRS J. Photogramm. Remote Sens. 132, 119–139.
Roperch, P., Sempere, T., Macedo, O., Arriagada, C., Fornari, M., Tapia, C., García, M., Laj, C., 2006. Counterclockwise rotation of late Eocene-Oligocene fore-arc deposits in southern Peru and its significance for oroclinal bending in the Central Andes: Paleomagnetic results for Peru. Tectonics 25 n/a-n/a.
Scharer, K.M., Biasi, G.P., Weldon, R.J., 2011. A reevaluation of the Pallett Creek earthquake chronology based on new AMS radiocarbon dates, San Andreas fault, California. J. Geophys. Res. 116, B12111.
Scholz, C.H., 1994. A reappraisal of large earthquake scaling. Bull. Seismol. Soc. Am. 84, 215–218. https://doi.org/10.1785/BSSA0840010215.
Silgado (1978) Silgado, E., 1978. Historia de los sismos más notables ocurridos en el Perú (1513 -1974) - [Boletín C 3]. Inst. Geológico Min. Met. - INGEMMET.
Steffen, D., Schlunegger, F., Preusser, F., 2009. Drainage basin response to climate change in the Pisco valley, Peru. Geology 37, 491–494.
Stirling, M., Goded, T., Berryman, K., Litchfield, N., 2013. Selection of Earthquake Scaling Relationships for Seismic-Hazard AnalysisSelection of Earthquake Scaling Relationships for Seismic-Hazard Analysis. Bull. Seismol. Soc. Am. 103, 2993–3011.
Thompson, S.C., Weldon, R.J., Rubin, C.M., Abdrakhmatov, K., Molnar, P., Berger, G.W., 2002. Late Quaternary slip rates across the central Tien Shan, Kyrgyzstan, Central Asia. J. Geophys. Res. Solid Earth 107. https://doi.org/10.1029/2001JB000596. ETG 7-1-ETG 7-32.
Thouret, J.-C., Davila, J., Eissen, J.-P., 1999. Largest explosive eruption in historical times in the Andes at Huaynaputina volcano, a.d. 1600, southern Peru. Geology 27, 435–438.
Thouret, J., Juvigné, É., Gourgaud, A., Boivin, P., Dávila, J., 2002. Reconstruction of the AD 1600 Huaynaputina Eruption Based on the Correlation of Geologic Evidence with Early Spanish Chronicles.

Villegas-Lanza, J.C., Chlieh, M., Cavalié, O., Tavera, H., Baby, P., Chire-Chira, J., Nocquet, J.-M., 2016. Active tectonics of Peru: Heterogeneous interseismic coupling along the Nazca megathrust, rigid motion of the Peruvian Sliver, and Subandean shortening accommodation: active Tectonics of Peru. J. Geophys. Res. Solid Earth 121, 7371–7394.

Wells, D.L., Coppersmith, K.J., 1994. New empirical relationships among magnitude, rupture length, rupture width, rupture area, and surface displacement. Bull. Seismol. Soc. Am. 84, 974–1002.

Westoby, M.J., Brasington, J., Glasser, N.F., Hambrey, M.J., Reynolds, J.M., 2012. 'Structure-from-Motion' photogrammetry: a low-cost, effective tool for geoscience applications. Geomorphology 179, 300–314.

Zaro, G., Nystrom, K.C., Keefer, D.K., 2013. Environmental catastrophe and the archaeological record: complexities of volcanism, floods, and farming in South Coastal Peru, AD 1200-1700. Andean Past 11, 17.